Bio-porphyrin supported single-atom iron catalyst boosting peroxymonosulfate activation for pollutants degradation: A Singlet Oxygen-dominated nonradical pathway

Yunlong Liu [a], Hongyan Zhou [a], Can Jin [a,*], Chunmei Tang [b], Wei Zhang [c], Guifeng Liu [a], Liang Zhu [c], Fuxiang Chu [a,*], Zhenwu Kong [a,*]

[a] *Institute of Chemical Industry of Forest Products, CAF, National Engineering Research Center of Low-Carbon Processing and Utilization of Forest Biomass, Key Lab. of Chemical Engineering of Forest Products, National Forestry and Grassland Administration, Nanjing 210042, China*
[b] *College of Science, Hohai University, Nanjing 210098, China*
[c] *College of Environment, Key Laboratory of Integrated Regulation and Resources Development of Shallow Lakes, Hohai University, Nanjing 210098, China*

ARTICLE INFO

ABSTRACT

Simultaneous modulation of the coordination environment of single-atom catalysts (SACs) and the construction of architectures with optimized exposed active sites are effective strategies to boost peroxymonosulfate (PMS) activation. Herein, the single-atom Fe supported on bio-sourced porphyrin-based porous active carbon (Fe-PAC) was reported with high porosity and abundant active sites. In particular, Fe-PAC showed high adsorption capacity (1892.7 mg g^{-1}) and enhanced PMS activation for degrading 96.1 % sulfamethazine (SMT) even in complicated environmental interference. The reactive oxygen species analytic experiments revealed that the Fe-PAC achieved high $^1O_2$ generation selectivity by activating PMS, which was confirmed by density functional theory (DFT) calculations results. The single Fe atoms were verified to serve as the dominant sites to activate PMS via the single O of SO_4^{2-}, yielding $^1O_2$ through pathway PMS → OH* → O* → OOH* → $^1O_2$. Therefore, the Fe-sites-generated $^1O_2$ could directly degrade the N-coordination sphere-adsorbed and pore-filling SMT with enhanced decontamination efficiency. This study sheds new insights on PMS activation mechanisms over single-atom metals-carbonaceous materials, thus promote its application for environmental remediation.

1. Introduction

Antibiotics have been defined as a unique group of recalcitrant organic pollutants (ROPs) due to their abuse and potential negative consequences both on public health and ecosystems [1,2]. Sulfamethazine (SMT), one kind of the most frequently used and broadly effective antibiotics [3], has drawn increasing concerns for its potential risks of biological resistance and resistant genes [4]. Unfortunately, the conventional wastewater treatment technologies, such as adsorption, biodegradation, chlorination, membrane filtration and ozone oxidation [5–7], still exhibit unsatisfactory efficient for SMT removal due to its sophisticated structure, harsh biodegradation requirements and various kinds of toxic degradation by-products [8,9]. Therefore, seeking effective technology to achieve rapid removal and mineralization of SMT remains a great challenge.

Peroxymonosulfate (PMS)-based advanced oxidation processes (AOPs) have been receiving tremendous attention as a clean and efficient approach for ROPs remediation [10]. Compared to other conventional oxidants, PMS is more easily to be activated for ROPs degradation, which relies on the presence of highly reactive radicals ($\bullet OH$, $SO_4^{\bullet-}$ and $O_2^{\bullet-}$) or nonradical ($^1O_2$) species [11–13]. Compared with free radical oxidation species, the nonradical singlet oxygen ($^1O_2$) species has been found to exhibit promising oxidation advantages including long life, broad pH tolerance, strong electrophilicity and high selectivity [14–16]. Nevertheless, wastewater treatment with PMS-based AOPs technology is typically conducted at low pollutant concentrations with limited degradation capacity due to the low $^1O_2$ generation and poor availability. Therefore, enhancing selective production of such reactive oxygen species (ROSs) and fully utilized of them is urgently required to mitigate the potential risks associated with high pollutant concentrations. Generally, the degradation process of pollutant in PMS system mainly involves capturing electrons from the active sites of activators,

---

weakening the chemical bonding energy, and breaking down the HSO_5^- to form $^1O_2$, transferring $^1O_2$ to pollutant, and resulting in degradation [14,17]. Thus, the $^1O_2$-dominant PMS system mainly relies on two aspects: enhancing activities of active sites for electron transferring in catalyst, and maximizing active sites exposure to reaction media, which facilitates the interaction between $^1O_2$ and the target pollutant molecules [18–20].

Single-atom metals supported on carbon substrates (SAMCs) have been emerged at the research frontier in catalysis reaction for their high atomic utilization efficiency, well-defined structures and satisfactory reactivities [21,22]. In SAMCs networks, metal atoms were directly coordinated with carbon support, which prevented the isolated metal atoms from aggregating and sintering into clusters or particles [23], as well as regulated the charge redistribution to modulate the reaction pathway towards $^1O_2$ production. Heteroatom doping modification (such as N, S, and P atoms) could equally tailor the catalytic electronic structure of carbon network, and thus significantly enhance $^1O_2$ generation selectivity from PMS activation [24]. Typically, introducing organic linkers to anchor metal atoms in precursors via coordination bonds is one of the most effective approaches to fabricate SAMCs. Besides the structure issue, the building block for traditional organic linkers such as 2-methylimidazole and 1,10-phenanthroline were widely used in SAMCs preparation [25,26]. Nevertheless, these linkers are mostly originated from fossil energy sources, which show potential risky to the ecological environment. Hence, searching for sustainable and green alternatives is on the agenda.

Taking into consideration these factors discussed above, the application of biomass-inspired SAMCs was thus expected to effectively improve PMS-based catalysis system. Vanillin, a biobased compound from lignin via biorefining process [27–29], was thus chosen as a green building block to prepare SAMCs precursor. Furthermore, a clear cognition on the reactive sites of biomass-inspired SAMCs for PMS adsorption and decomposition is highly demanded for further understanding the catalytic mechanism in PMS-based AOPs, which would shed light on the development of other biobased catalysts. Hence, in this study, the bio-sourced single-atom Fe-porphyrin-based activated carbon (Fe-PAC) was firstly synthesized by hydrothermal treatment in the presence of Fe (III) and followed pyrolysis from vanillin-based porphyrin. Characterizations of materials were used to illustrate the porosity structure, nitrogen configuration, defective degree and dispersibility of Fe atoms. The adsorption and degradation of high concentration SMT by Fe-PAC/PMS system was systematically investigated. Furthermore, DFT calculations were performed to achieve a further insight into the catalytic mechanism. Finally, the possible degradation products of SMT and their potential toxicity were also discussed.

2. Experimental section

2.1. Chemicals

Iron (III) chloride hexahydrate ($FeCl_3 \bullet 6H_2O$, 99 %), vanillin (99 %), pyrrole (99 %), sulfamethazine (SMT, 98 %), peroxymonosulfate (PMS, 98 %), acetic acid, potassium hydroxide (KOH), anhydrous methanol, anhydrous ethanol (EtOH), sodium hydroxide (NaOH), sodium chloride (NaCl), sodium sulphate (Na_2SO_4), sodium dihydrogen phosphate (NaH_2PO_4), sodium carbonate ($NaHCO_3$), sodium nitrate ($NaNO_3$), D_2O (99.9 %) and humic acid (HA) were purchased from Adamas Corporation (Shanghai, China). Laccase from Trametes Versicolor (120 U g^{-1}) was bought from Sigma-Aldrich. All chemicals were used without further purification.

2.2. Synthesis of Fe-porphyrin-based porous organic polymer

In this procedure, the vanillin dimer (divanillin) was first prepared according to our previous work [30]. Detailed information was listed in Text S1 in the Supporting Information (SI) part. The Fe-porphyrin-based porous organic polymer (Fe-PPOP) was prepared with a facile solvothermal method. Typically, divanillin (0.61 g, 2.0 mmol) and pyrrole (0.27 g, 4.0 mmol) were dispersed into 150 mL acetic acid under magnetic stirring for 10 min. Then, the calculated amounts of $FeCl_3 \bullet 6H_2O$ were added to the solution and vigorously stirred for 4 h at room temperature. Afterward, the black suspension was transferred into a 200 mL Teflon-lined stainless-steel autoclaves and then heated at 180 °C for 72 h. The resulting precipitates were collected through filtration and washed in sequence with N, N-dimethylacetamide (DMAC), tetrahydrofuran (THF), acetone, EtOH and water, and finally dried at 70 °C for 12 h to get Fe-PPOP-X, where X referred to the introduced amount of $FeCl_3$ (0, 1.0, 2.0, 4.0 and 8.0 mmol, respectively), namely, PPOP, Fe-PPOP-1, Fe-PPOP-2, Fe-PPOP-4, and Fe-PPOP-8, respectively.

2.3. Synthesis of Fe-porphyrin-based activated carbon

The Fe-porphyrin-based activated carbon (Fe-PAC) was prepared by pyrolyzing the Fe-PPOP obtained in the previous step. Typically, 2.0 g Fe-PPOP were thoroughly mixed with 4.0 g KOH, and then pyrolyzed in a tubular furnace at 800 °C for 2 h under the N_2 atmosphere. After natural cooling, the carbon product was etched by 0.5 M HCl for 12 h and then the black powder was washed with deionized water until the solution pH to be neutral, then dried at 60 °C for 8 h to obtain the catalysts. The catalysts prepared from various Fe-PPOP were respectively labelled as PAC, Fe-PAC-1, Fe-PAC-2, Fe-PAC-4 and Fe-PAC-8, respectively. The Fe-porphyrin-based porous carbon (Fe-PPC) was prepared during the same process except did not add KOH.

2.4. Adsorption and catalytic experiments

The adsorption experiments were carried out in the 150 mL conical flasks with predesigned concentrations of SMT (100 mL, 5–500 mg/L) solution and adsorbents dosage (0.1 g/L). The mixture was stirred at 25 °C for 10 h to get sufficient contact. At selected time intervals, 2.5 mL suspensions were sampled, separated through a 0.22 μm membrane filter and then analyzed on a UV–vis spectrophotometer (INESA Co., Ltd, China) at 262 nm. The adsorption behavior of SMT on Fe-PAC was investigated by kinetic and isotherm modeling studies. For the desorption experiments, the SMT-saturated Fe-PAC (5 mg) was collected after conducting adsorption experiment, following stirred in 100 mL methanol for 60 min. And the eluent was analyzed in the same way as in the adsorption process.

The catalytic properties of Fe-PAC for SMT were carried out in a 150 mL conical flask at 25 °C. Typically, 5.0 mg Fe-PAC was added to 100 mL SMT solution (100 mg/L, pH 6.9 without adjusting) and stirred for 30 min to achieve adsorption-desorption equilibrium. Subsequently, a specific dosage of PMS was added to begin the degradation reaction. At selected time intervals, 2.5 mL of the reaction solution was withdrawn and immediately detected by the UV spectrophotometer. The reaction standard curve was obtained by probing the concentration of SMT based on Lambert-beer's law, and the reaction rates were estimated by the pseudo-first-order equation (Table S1). After degradation, desorption experiments were further performed as previously to investigate the degradation of SMT adsorbed on the catalyst. The effects of catalyst dosage, PMS concentration, SMT concentration, solution pH and reaction temperature were investigated on the performance of Fe-PAC/PMS system for SMT removal. The water qualities with inorganic ions, HA and different water environments were also simulated to study the practicability of Fe-PAC. For the quenching of various free radicals, methanol, tert-butanol (TBA), chloroform (CF), furfuryl alcohol (FFA) and dimethyl sulfoxide (DMSO) were used as quenchers for different radicals.

3. Results and discussion

3.1. Characterization

Briefly, the divanillin molecule was firstly performed from vanillin monomer in the presence of laccase, then was applied to react with pyrrole by condensation reaction to form the porphyrin-based porous organic polymers (PPOP) [31]. The porphyrin units could be further coordinated with Fe ions resulting in the formation of Fe-PPOP [32]. Finally, the Fe-PPOP was mixed with KOH and carbonized at 800 °C in N_2 atmosphere to obtain a porous, N-doped and single-atom Fe-porphyrin-based activated carbon (Fig. 1a).

The existences of aromatic ring and porphyrin functionality in PPOP and Fe-PPOP were confirmed from FT-IR and ^{13}C NMR spectra (Fig. S1). The absence of C=O stretching band of divanillin at 1720–1740 cm^{-1} indicated the full conversation of aromatic aldehyde. The presence of absorption bands such as 1590 cm^{-1} (C=N stretching of porphyrin macrocycle), 1459 and 1408 cm^{-1} (phenyl ring C=C vibrations) and 1258 cm^{-1} (C-N deformation vibration of porphyrin macrocycle) confirmed the formation of porphyrin-based macrocycles from the combination of pyrrole and divanillin (Scheme 1, Fig. S1a). Notably, the C-N vibrations in the Fe-PPOP spectrum exhibited a significant blue-shift in relation to that in PPOP, which could be due to the presence of Fe species in the porphyrin ring of Fe-PPOP. Moreover, the appearance of a distinct vibration at 1077 cm^{-1} also represented the Fe (III) chelation in the porphyrin cavity, which afforded the framework of Fe-PPOP [31, 33]. Furthermore, the solid-state ^{13}C NMR spectral analysis of PPOP and Fe-PPOP (Fig. S1b) revealed a broad peak at 100–150 ppm, respectively, which assigned to the sp^2-hybridized carbons of the aromatic phenyl and porphyrin units [34], agreeing with the observation in the FT-IR spectroscopy. In addition, the sharp signal at 55 ppm was observed for PPOP and Fe-PPOP, which was assigned to methyl carbon resonances of methoxy groups [35] (Fig. S1b).

The X-ray photoelectron spectroscopy (XPS) spectra confirmed the presence of C, O, N and Fe elements in Fe-PAC (Fig. S2a and Table S2). As shown in Fig. 2a, N 1s spectrum of Fe-PAC could be deconvoluted into four types of N configuration. Intriguingly, pyrrolic N species were the dominant N species in Fe-PAC-2, which could provide coordination sites for Fe atoms in carbon networks as potential active sites for pollutant adsorption and electron transferring [19]. Furthermore, a mild shift of pyrrolic N peak could be noticed between PAC and Fe-PAC (Fig. S2b), confirming the coordination between Fe atoms and pyrrolic N species [36]. For Fe 2p XPS spectra of Fe-PAC-2 (Fig. 2b), two peaks appeared at 708.74 eV and 721.80 eV, which were indexed to Fe 2p$_{3/2}$ and Fe 2p$_{1/2}$, respectively, with satellite peaks at 715.62 eV and 730.16 eV. Further deconvolution revealed that peaks located at 708.98 and 721.98 eV were attributed to Fe^{2+}, while peaks at 712.14 and 725.94 eV were assigned to Fe^{3+}, and no peaks related to Fe^0, suggesting the formation of atomically dispersed Fe atoms in Fe-PAC-2 network [37]. X-ray diffraction (XRD) patterns exhibited the carbon matrix of Fe-PAC (Fig. S2c). No characteristic peaks associated with Fe oxides could be observed in Fe-PAC, indicating the crystalline and oxide Fe containing species were not formed or have been eluted after acid leaching [37]. Moreover, it could be noted that as the Fe-doping content increased, the sharp diffraction peaks gradually appeared, which could be attributed to the aggregation of excess Fe in Fe-PAC matrix, indicating that the overloaded of Fe was not conducive to the production of atomically dispersed Fe atoms in the catalysts. The larger I_D/I_G value of Fe-PAC-2 from the Raman spectra (Fig. S2d) demonstrated that Fe-PAC-2 exhibited more defective structure, edges or topologic defects and declined sp^2 carbon than other catalysts, which was conducive to electronic transmission [11]. The lower value of I_D/I_G indicated the higher the degree of graphitization of Fe-PAC-1, Fe-PAC-4, and Fe-PAC-8, which probably as a result of the catalytic function of Fe during pyrolysis [38,39].

The morphology and microstructure of Fe-PAC-2 were examined by SEM (Fig. S3a-c) and HR-TEM (Fig. S3d-f). Fe-PAC-2 exhibited a honeycomb-like porous structure, which would provide sufficient contact areas for catalytic reaction and expose more active sites during AOPs. No obvious nanoparticles lattices were observed from the HR-TEM images, verifying the absence of metal oxides for Fe-PAC-2 [40]. Fig. 1b-c displayed the aberration-corrected high-angle annular dark field scanning transmission electron microscopy (AC HAADF-STEM) images with various magnifications. The abundant isolated bright dots (highlighted by red circles) in the porous carbon matrix provided direct
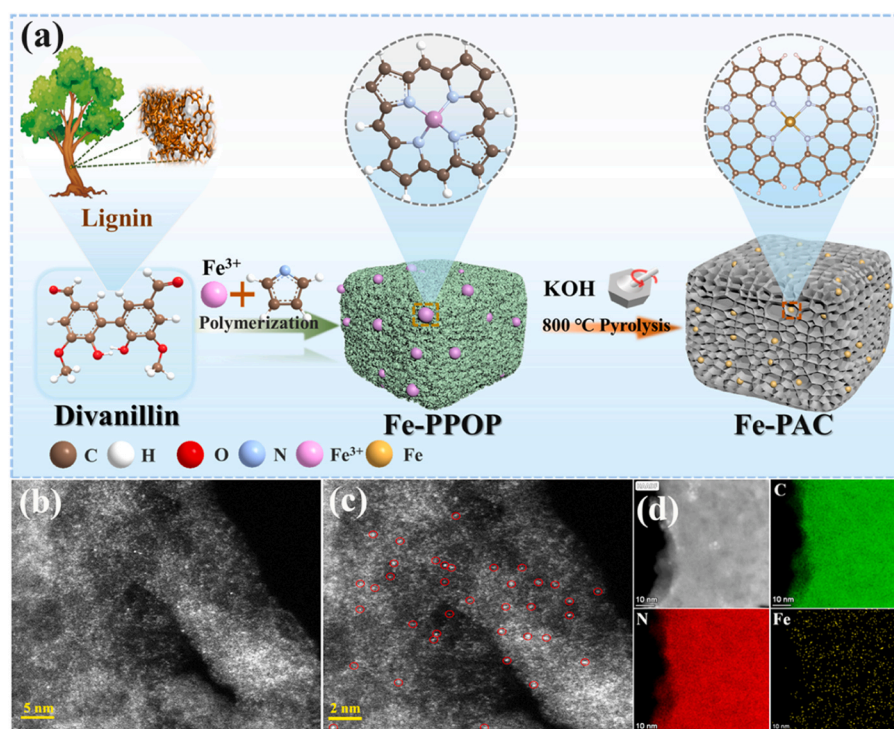

Fig. 1. (a) Synthesis of Fe-PAC from divanillin compound, (b-c) AC-HAADF-STEM, (d) EDS mapping images of Fe-PAC-2.
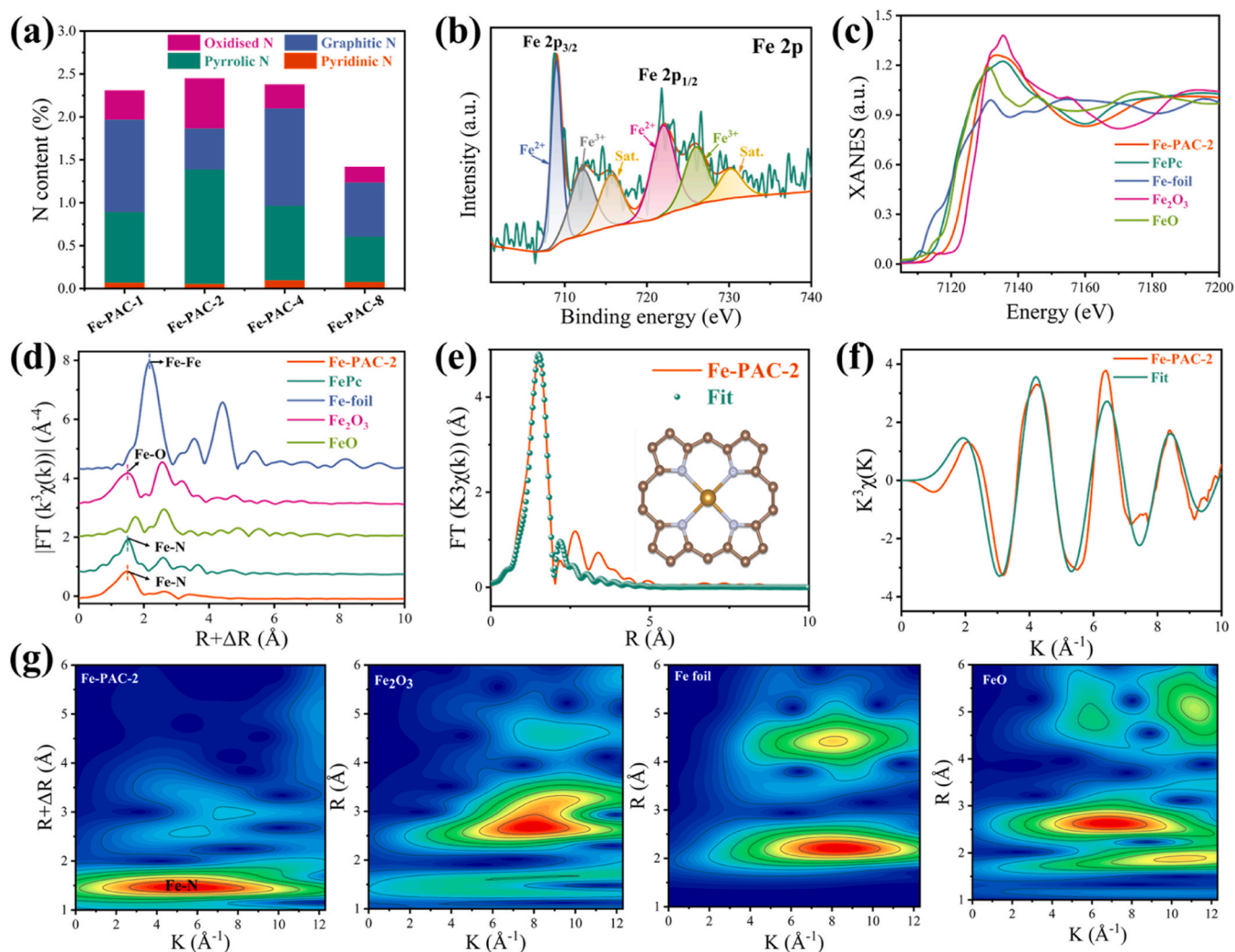
Fig. 2. (a) Fe 2p XPS spectra of Fe-PAC-2. (b) the corresponding N contents of different catalyst (c-d) Fe K-edge XANES spectra and FT-EXAFS signal of Fe-PAC-2 and reference samples. Quantitative EXAFS fitting curve at (e) R space and (f) *k* space. (g) Co K-edge WT EXAFS contour plots for Fe-PAC-2, Fe₂O₃, Fe foil and FeO.

evidence for the atomically dispersion Fe throughout the entire Fe-PAC-2 architecture. The energy dispersive X-ray (EDS) elemental mapping further identified the homogeneous distribution of C, N and Fe elements in the catalysts (Fig. 1c), where the Fe content of Fe-PAC-2 was about 0.65 wt% determined by inductively coupled plasma optical emission spectrometry (ICP-OES). These results of HAADF-STEM and EDS elemental mapping analysis both approved the successful fabrication of single-atom Fe catalyst.

X-ray absorption fine structure (XAFS) measurements were further conducted to identify the possible chemical state and coordination environment of single Fe atoms in Fe-PAC-2. The absorption edge of Fe-PAC-2 was located between FeO and Fe₂O₃ references in Fe K-edge Xray absorption near-edge structure (XANES) spectra (Fig. 2c), indicating that the Fe atom was an oxidation state between Fe^{2+} and Fe^{3+}. The formation of Fe-N bonds in Fe-PAC-2 was confirmed by the k^3-weighted Fourier transform extended X-ray absorption fine structure spectra (FT-EXAFS) in Fig. 2d. A main peak at 1.47 Å of Fe-PAC-2 corresponded to the Fe-N bond, and no obvious Fe-Fe peak at 2.17 Å or other high-shell peaks was observed, manifesting the atomic Fe dispersed on Fe-PAC-2. The EXAFS fitting curves for Fe-PAC-2 was shown in Fig. 2e and f, and the corresponding quantitative structural parameters were given in Table S3. The atomic Fe site in Fe-PAC-2 showed a coordination number of 4.1 and a bond length of 1.98 Å, indicating that the single Fe atoms were coordinated in a graphene plane with four pyrrolic N. The wavelet

transforms (WT) contour plots (Fig. 2g) of Fe-PAC-2 revealed a WT maximum at ≈ 4.2 Å⁻¹, which could be assigned to Fe-N bond and no intensity maximum corresponding to Fe-Fe was observed. According to these results, it could be concluded that the Fe-PAC-2 with robust single-atom FeN₄ sites was successfully fabricated.

The N₂ adsorption-desorption isotherms of Fe-PPOP, Fe-PPC and Fe-PAC-2 were provided in Fig. S4a, which suggested that all those catalysts showed hierarchically porous structures [41]. The S_BET of Fe-PPOP was 41.2 m² g⁻¹, and slightly increased to 61.7 m² g⁻¹ for Fe-PPC after carbonization at 800 °C (Table S4). Compared with Fe-PPC, the S_BET increased to 2612.7 m² g⁻¹ using KOH as porogen at 800 °C and the pore volume expanded from 0.074 to 1.361 m³ g⁻¹ for Fe-PAC-2. Moreover, the pore size distribution curves (Fig. S4b) demonstrated that the pore diameter of Fe-PAC-2 mainly located at 0.8–16.0 nm, verifying a hierarchical porous structure. Therefore, the high S_BET and porous structure would facilitate Fe-PAC-2 as a promising activator for PMS adsorption and activation.

3.2. Roles of porous architecture and Fe, N-doping on SMT removal

The obtained catalysts were evaluated for the adsorption and degradation of SMT. PMS was founded to hardly adsorb or degrade SMT in the whole treated time without addition of any catalysts (Fig. 3a), while PPOP, Fe-PPOP and Fe-PPC showed adsorption efficiency of 11.2
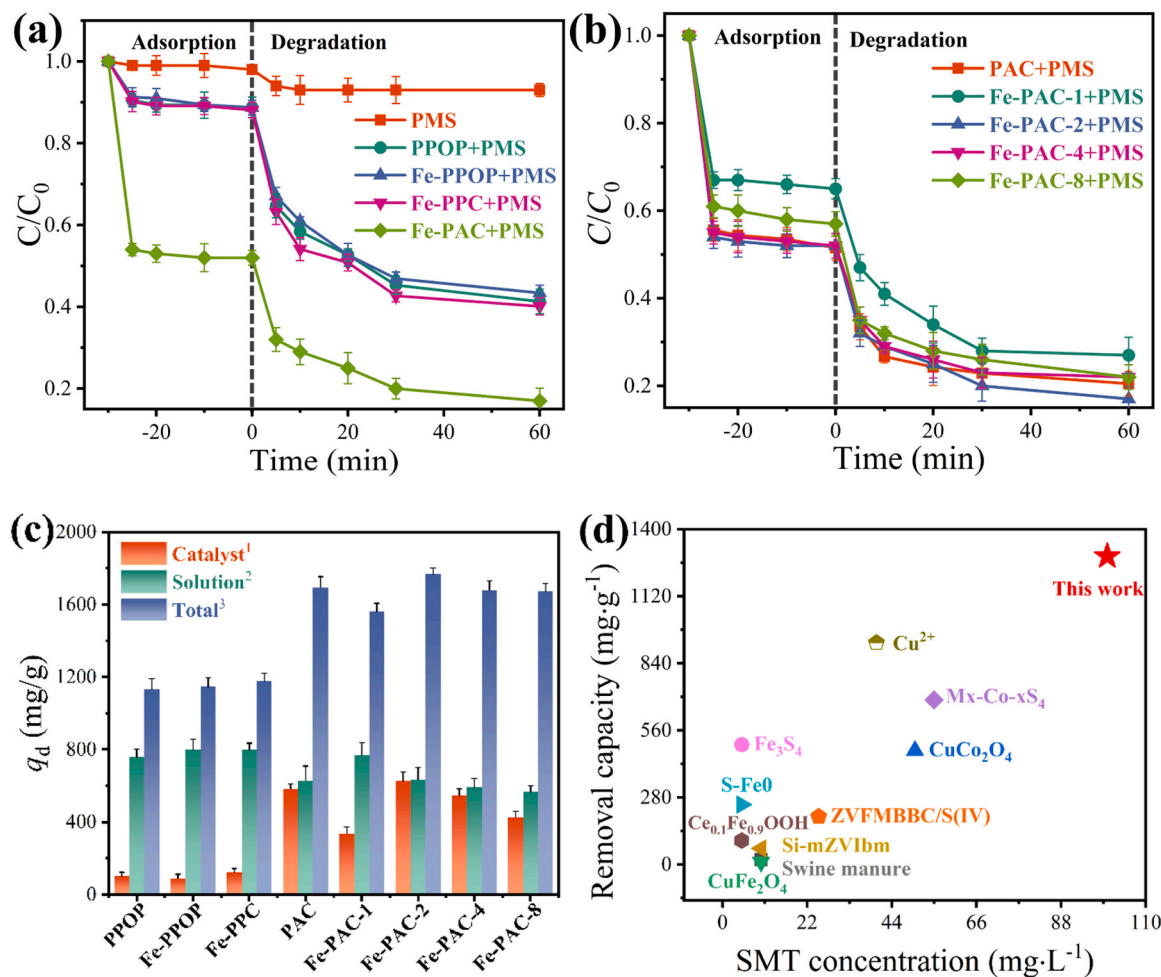
Fig. 3. (a-b) The removal of SMT in different reaction systems. (c) removal capacity of SMT on different catalysts. (d) the comparisons between Fe-PAC-2/PMS and other documented PMS-AOPs (Experimental conditions: catalyst dosage = 0.05 g L^{-1}, [SMT] = 100 mg L^{-1}, [PMS] = 0.5 mM, and reaction temperature = 25 °C). [1] The degradation capacity of SMT adsorbed on the catalysts; [2] The degradation capacity of SMT in the solution; [3] The total removal capacity (adsorption and degradation) of SMT.

%, 11.3 % and 11.9 % toward SMT, respectively. Interestingly, the presence of Fe-PAC-2 resulted in over 46.5 % adsorption efficiency for SMT within 5 min. The adsorption efficiency of different catalysts follows the order of Fe-PAC-2 > Fe-PPC > Fe-PPOP > PPOP, which matched well with the order of samples porosities. Detailed investigation on the adsorption properties of Fe-PAC-2 could be found in Text S4 and Fig. S5 in SI. Remarkably, 83.5 % of SMT could be removed by adding PMS in the presence of Fe-PAC-2 catalyst even at a high SMT concentration (100 mg L^{-1}), whereas the removal rates could only reach 58.7 %, 56.6 % and 59.9 % for the addition of PPOP, Fe-PPOP and Fe-PPC catalysts, respectively (Fig. 3a), indicating that the high S$_{BET}$ of Fe-PAC-2 highly facilitated the adsorption and degradation of SMT.

The roles of single-atom Fe, N-doping on PMS activation were further investigated by constructing Fe-PAC catalyst with different contents of Fe and N elements. As shown in Fig. 3b, the adsorption and degradation rate of Fe-PAC significantly enhanced with the increase of Fe loading content from 1.0 to 2.0 mmol, and subsequently decreased when the Fe loading content continuously increased from 2.0 to 8.0 mmol, which could be attributed to the aggregation of Fe nanoparticles. Moreover, the SMT removal rate increased with the increment of pyrrolic N content (Fig. 2a and 3 b), which indicated that the SMT removal property mainly relies on the single-atoms Fe sites and pyrrolic N content of Fe-PAC materials. The degradation performance of the SMT adsorbed on catalysts were also examined by desorption experiments (Fig. 3c). Results showed that the generated ROSs from Fe-PAC-2/PMS system could not

only degrade SMT from solution, but could also degrade around 80 % of the SMT adsorbed on Fe-PAC-2 (Fig. 3c), which indicated that the SMT-adsorbed Fe-PAC-2 could be in-situ regenerated in the presence of PMS. Thus, the removal capacity of the catalysts/PMS systems covered the adsorption capacity of SMT, the degradation capacity of SMT adsorbed on the catalyst and the degradation capacity of SMT in the solution. Thus, the removal capacity of Fe-PAC-2 for SMT was found to be 1767.2 mg/g, which was higher than those of Fe-PAC-1, Fe-PAC-4 and Fe-PAC-8 with in 1561.5 mg/g, 1680.3 mg/g and 1673.5 mg/g, respectively (Fig. 3c). Remarkably, the activity of Fe-PAC-2 for high concentration SMT degradation had by far surpassed most of the reported materials (Fig. 3d). Moreover, the total organic carbon (TOC) analysis results showed removal rate reached approximately 64.0 % within 60 min (Fig. S5d), indicating the high mineralization capability of Fe-PAC-2/PMS system for SMT. Therefore, based on the above findings, Fe-PAC-2 was adopted for the following tests and mechanism exploration. [42–51].

3.3. Influences of various factors on SMT catalytic degradation

To further verify the PMS activation ability of Fe-PAC-2, several comparative experiments were conducted under different testing conditions. The effect of Fe-PAC-2 dosage on SMT removal properties was firstly evaluated (Fig. 4a and S6a). The removal rate increased from 76.3 % to 96.1 % as the Fe-PAC-2 dosage increased from 0.05 to 0.15 g L^{-1},
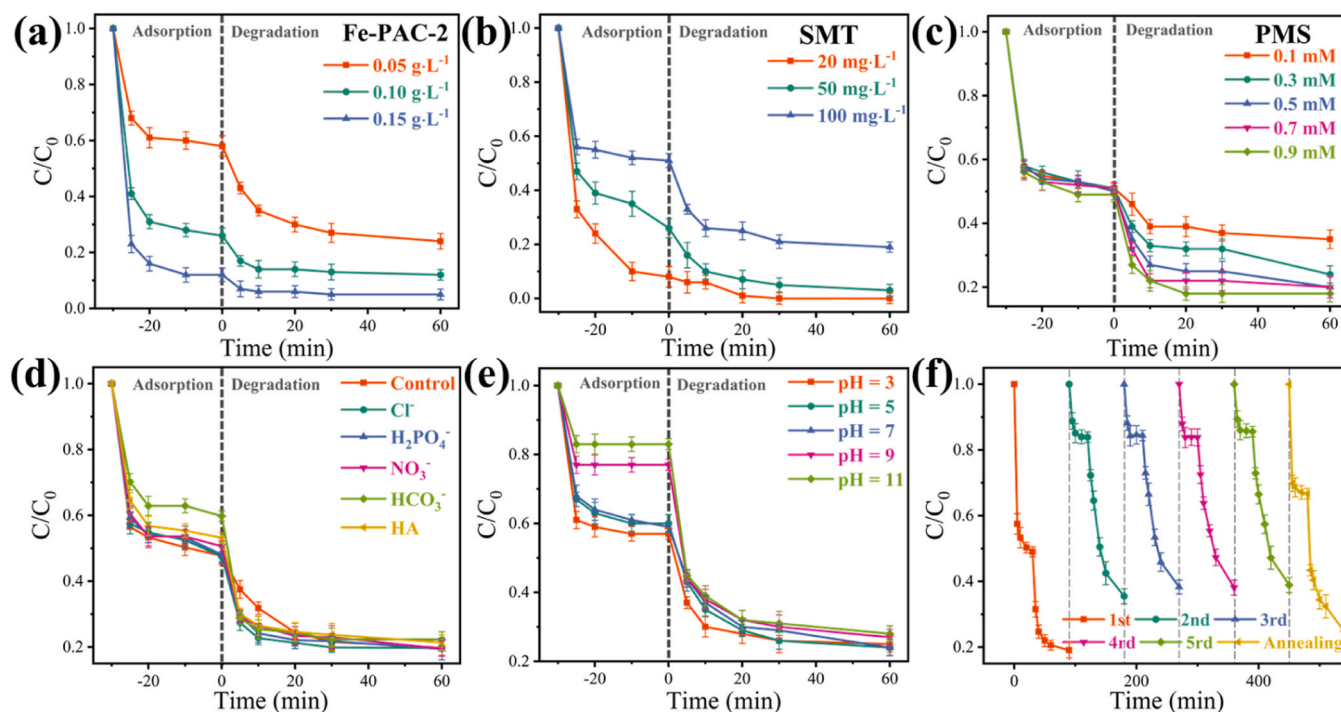
Fig. 4. Effect of (a) catalyst dosage, (b) SMT concentration, (c) PMS concentration, (d) inorganic ions/HA, (e) solution pH, (f) reusability of Fe-PAC-2 on removal capacity of SMT. (Experimental conditions: Fe-PAC-2 dosage = 0.05 g L^{-1}, [SMT] = 100 mg L^{-1}, and [PMS] = 0.5 mM, T = 25 °C, [Cl^-] = [HCO_3^-] = [NO_3^-] = 10 mM, [HA] = 10 mg L^{-1}).

while the removal capacity decreased from 1675.5 to 703.4 mg g^{-1}, indicating the excess active sites supplied by a larger Fe-PAC-2 dosage [19]. As illustrated in Fig. 4b and S6b, the removal efficiency of Fe-PAC-2 varied with different SMT concentrations: almost 100 % of SMT was removed at low concentration (20 mg L^{-1}), and gradually decreased to 97.3 % as the SMT concentration increased from 20 to 50 mg L^{-1}, which indicated the outstanding removal ability of Fe-PAC-2 at a wide range of SMT concentrations. As SMT concentration continuously increased, the adsorption and degradation capacity of SMT by Fe-PAC-2 both increased significantly and the whole removal capacity was 1730.6 mg g^{-1} at SMT concentration of 100 mg L^{-1}, illustrating the excellent decontamination performance even at high SMT concentration. In addition, the increment of PMS concentration (from 0.1 to 0.5 mM) considerably promoted the SMT removal rate from 64.5 % to 79.6 % (Fig. 4c and S6c). Then the removal efficiency slightly increased from 79.6 % to 81.5 % as the PMS concentration increased from 0.5 to 0.9 mM. An explanation for this phenomenon could be that more PMS molecules were adsorbed onto Fe-PAC-2 sites, thus generated more available ROSs for SMT degradation [52]. Ordinarily, the reaction temperature also performed a vital role in PMS-based AOPs. The adsorption performance improved from 1030.1 to 1139.8 mg g^{-1} as the temperature raised from 15 to 45 °C (Fig. S6d), and the standard enthalpy (ΔH^o) was 5.41 kJ/mol as shown in Table S9, suggesting the endothermic nature of SMT adsorption. Moreover, the degradation capacity of Fe-PAC-2/PMS system correspondingly increased from 988.9 to 1125.6 mg g^{-1} (Fig. S6e), manifesting that the higher temperature was beneficial for SMT degradation reaction.

3.4. Environmental application evaluation

Generally, multiple coexisting matters, such as Cl^-, $H_2PO_4^-$, NO_3^-, HCO_3^- and humic acid (HA) in actual waterbody, can perturb some free radicals, especially $^{\bullet}OH$ and $SO_4^{\bullet-}$, resulting in the decrement of removal efficiency for AOPs (Text S5). Therefore, the effects of typical inorganic anions and HA at different concentrations on SMT degradation were investigated in detail. Strikingly, these anions in water had minor effect on SMT degradation even at high concentration (Fig. 4d, S7 and S8a), and the removal capacities were all around 1750 mg g^{-1}, indicating that the generation of ROSs and the subsequent degradation of SMT were basically unaffected by common organic and inorganic substance presenting in water [11,14]. Consequently, SMT removal in the Fe-PAC-2/PMS system under different initial pH was investigated. Remarkably, Fe-PAC-2 catalyst exhibited not only excellent reactivity under acidic and neutral conditions (Fig. 4e and S8b, around 76.0 % SMT removal), but also impressive reactivity under alkaline conditions (more than 72.0 % SMT removal). And the total SMT removal capacities were all around 1675.5 mg g^{-1} in the whole pH range (Fig. S8b and S9). These results showed broad pH compatibility for the Fe-PAC-2 catalyst in PMS-based AOPs for practical application.

The effect of Fe-PAC-2 on SMT removal in different water was simulated to further investigated the utility of Fe-PAC-2 in the environment. The SMT adsorption rates of tap water and lake water were 47.4 % and 40.4 %, which was appreciably lower than deionized water (52.3 %, Fig. S8c-d). This might be attributed to the presence of inorganic ions in the tap water that had not been completely treated, as well as some organic contaminants in the lake water [52]. Intriguingly, the comparable removal rates of SMT in the three aqueous mediums indicated that Fe-PAC-2/PMS system had outstanding degradation performance at different aqueous environment and exhibited potential application in treating actual wastewater. The efficient removal of other contaminants (e.g. bisphenol A (BPA), tetracycline (TC), ofloxacin (OFL), sulfadiazine (SDZ)) reflected the effectiveness of Fe-PAC-2 for catalyzing the degradation of a wide range of organic contaminants via PMS activation, despite the fact that an obvious difference in adsorption capacity of Fe-PAC-2 was exhibited for these contaminants (Fig. S8e). The results of reusability and stability experiments showed that Fe-PAC-2 maintained approximately 76 % of its original removal performance after the fifth cycles (Fig. 4f), indicating the long-term use potential of Fe-PAC-2. Moreover, Fe-PAC-2 was annealed at 800 °C for 1 h under N_2 atmosphere after five cycles, and the regenerated Fe-PAC-2

could also degrade SMT effectively in consecutive runs with performance comparable to that of the fresh catalysts, which indicated the satisfactory reusability and stability of Fe-PAC-2 catalyst in practical application.

3.5. Catalytic mechanisms

3.5.1. Identification of predominant ROSs

Quenching experiments were conducted to identify the dominated ROSs in the Fe-PAC-2/PMS system. MeOH was used as radical scavenger for both $^\bullet$OH and $SO_4^{\bullet-}$, and TBA was used as quenching agents for $^\bullet$OH (corresponding reaction rate constants were summarized in Table S10). As shown in Fig. 5a, both MeOH and TBA have a negligible inhibitory effect on the catalytic reaction, indicating that the radical $^\bullet$OH and $SO_4^{\bullet-}$ pathway contributed a small role in the catalytic performance. When CF (radical scavenger for $O_2^{\bullet-}$ and corresponding reaction rate constants were summarized in Table S10) was added into the reaction solution, only a slight inhibition ratio of SMT degradation could be observed (0.6 %), indicating that the major ROSs produced in PMS activation by Fe-PAC were not $O_2^{\bullet-}$. In addition, to examine the generation of high-valent Fe-oxo species (Fe(III) and Fe (IV)), the oxidation experiment of trans-stilbene to trans-stilbene oxide, a convention oxygen atom transfer reaction, was performed to evaluate the oxidation of high-valent iron-oxygen species [53]. If the oxygen atom transfer reaction predominated the reaction, it would convert trans-stilbene to trans-stilbene oxide with a fairly high selectivity [54]. The data in Fig. S10a indicated that the actual selectivity of trans-stilbene to trans-stilbene oxide was so low (2.27 %) that the importance of high valent iron oxidation could be almost disregarded. DMSO, which could reduce the high-valent iron-oxo species to Fe (II), was used as quenching agent [33]. The degradation efficiency of SMT was decreased from 80.9 % to 75.7 % after addition of DMSO (Fig. 5a). This slight inhibition of DMSO further verified the high-valent iron-oxo species played a minor role in the degradation of SMT. When L-histidine or FFA was applied, the degradation rate of SMT dramatically decreased from 80.9 % to 49.4 % or to 48.5 % (Fig. 5a), and

the SMT removal efficiency almost exclusively relied on the adsorption properties, implying that $^1O_2$ was the major ROSs in Fe-PAC-2/PMS system and played a dominant role during SMT degradation process. Actually, the typical $^1O_2$ scavenger of FFA or L-histidine can also react with PMS ineluctably, hindering the release of other ROS. The as-mentioned quenchers (L-histidine) tended to react with $^1O_2$ preferentially because $k_{1O2, \text{L-histidine}}$ (3.2×10^7 M^{-1} s^{-1}) is almost 10^7 times higher than $k_{PMS, \text{L-histidine}}$ (10.9 M^{-1} s^{-1}) [55]. Therefore, the results of quenching tests using L-histidine were still reliable. Thus, the overwhelming majority of $^1O_2$ in the Fe-PAC-2 system indicated that a non-radical process might occur during the activation of PMS [56].

The electron paramagnetic resonance spectrum (EPR) was used to gain more insight into the generated ROSs. The EPR spectra with only PMS did not exhibit any characteristic peak for radicals, indicating that no radicals were generated when PMS directly reacted with SMT [19]. While the formation of 5,5-dimethyl-2-pyrrolidone-N-oxyl (DMPOX) could be verified in Fe-PAC/PMS system (Fig. S10b), which could be attributed to the oxidation of 5,5-Dimethyl-1-pyrroline-N-oxide (DMPO). The strong oxidative substance was reported to produce DMPOX from over-oxidation of DMPO [56]. As the quenching experiments results indicated $^1O_2$ was the main ROSs in Fe-PAC/PMS system. Thus, DMPOX could be produced from the oxidation of DMPO by $^1O_2$. Furthermore, 2,2,6,6-tetramethylpiperidine (TEMP) was used as the trapping agent to confirm the presence of $^1O_2$. Three characteristic peaks of TEMP-$^1O_2$ were obviously observed in the EPR spectra, and the signal intensity continued to increase as the reaction progressed (Fig. 5b), indicating that Fe-PAC-2 could continuously activate PMS to form $^1O_2$ [14]. Electron transfer from organic compounds to PMS, facilitated by activator, could be responsible for another nonradical mechanism. To determine the existence of electron transfer process (ETP) in Fe-PAC-2/PMS system, electrochemical studies such as chronoamperometry (i-t) and linear sweep voltammetry (LSV) were employed. The addition of PMS generated an obvious impact on the current output (Fig. S10c), indicating the ETP between PMS and Fe-PAC-2 to form a metastable Fe-PAC-2/PMS complex. A significant
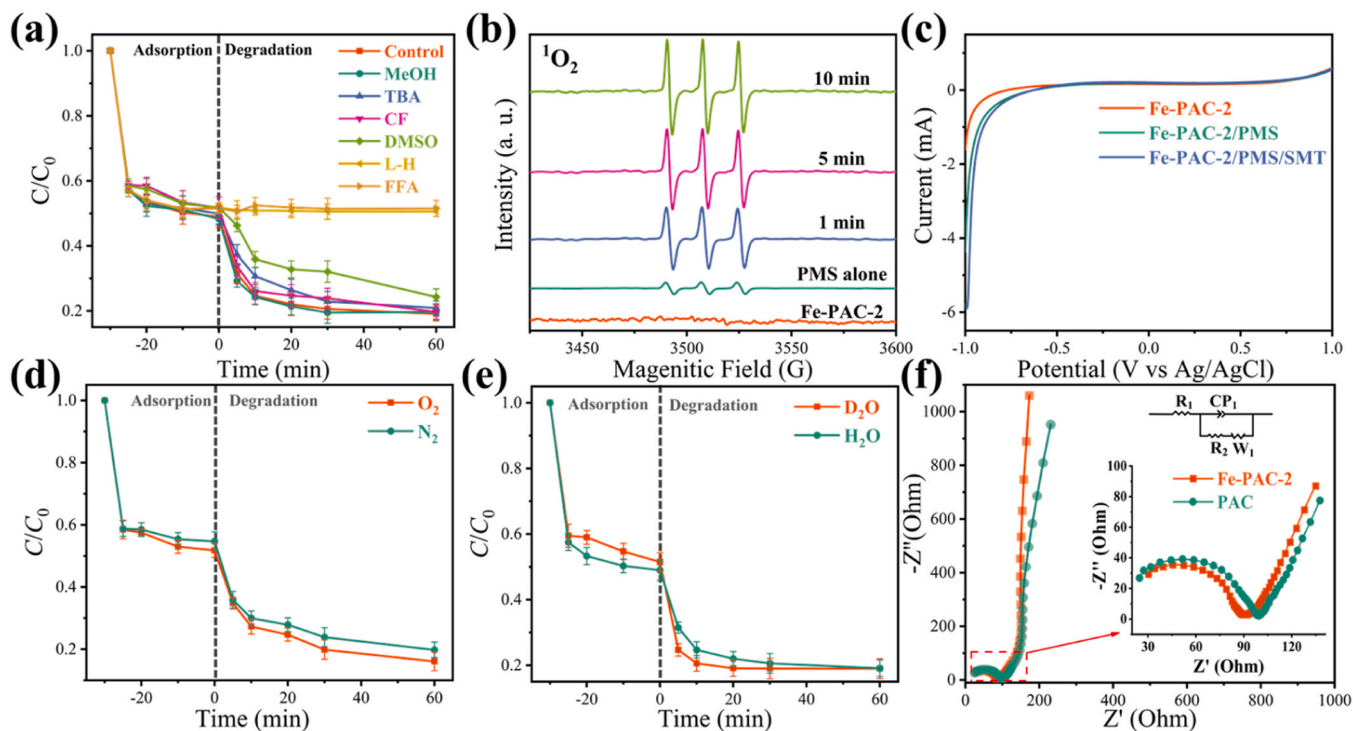

Fig. 5. (a) Inhibition effect of different quenchers on SMT removal. (b) EPR spectra of TEMP-$^1O_2$. The effects of (c) atmosphere (O_2 and N_2) and (d) reaction solvents (H_2O and D_2O) upon SMT removal in Fe-PAC-2/PMS system. (e) EIS analysis, (f) LSV analysis. (Experimental conditions: [Fe-PAC-2] = 0.05 g L^{-1}, [SMT] = 100 mg L^{-1}, T = 25 °C, [PMS] = 0.5 mM, [MeOH] = [TBA] = [CF] = 500 mM, [FFA] = [DMSO] = 20 mM).

decrease papered after adding SMT, confirming that Fe-PAC-2 could mediate the electron transfer from SMT to PMS effectively [3]. From the LSV plot (Fig. 5c), it is revealed that the addition of PMS and SMT gave lower current than adding only PMS or SMT, suggesting that electron transfer occurred between PMS and SMT through the Fe-PAC-2 [57]. Due to the limited lifetime of $^1O_2$ (2 μs), PMS was pre-mixed with Fe-PAC-2 for 30 min following SMT added into the system to verify the dominant role of $^1O_2$ in SMT removal [52,58,59]. If the system undergoes ETP mechanism, slight inhibition will be observed in the PMS pre-mixed system. However, as the SMT added into the PMS pre-mixed system, major inhibition to the SMT removal was observed in PMS pre-mixed system (Fig. S10d). And the main SMT removal mainly derived from the adsorption of Fe-PAC-2. Therefore, it can be concluded that the ETP contributed minor role in the SMT removal. Thus, the aforementioned results confirmed that $^1O_2$ acted as the major ROSs responsible for the degradation of SMT.

After clarifying the dominant role of $^1O_2$ in the Fe-PAC-2/PMS system, the $^1O_2$ generation process was further investigated. Typically, $^1O_2$ could be derived from the self-decomposition of PMS, dissolved oxygen, as well as mutual conversion with $O_2^{\bullet-}$ (Text S5). The atmospheres of O_2 and N_2 gas showed no significant effect on the degradation performance of SMT (Fig. 5c), suggesting that the O atom for $^1O_2$ was not generated from dissolved oxygen. The degradation of SMT was further carried out using D_2O as a solvent to investigate the ROSs in the Fe-PAC-2/PMS system. It had been verified that the lifetime of $^1O_2$ could be significantly extended in D_2O (20–32 μs) than in water (2 μs) [11], so for $^1O_2$ participated reactions, the contaminant degradation could be accelerated when H_2O was substituted by D_2O. Compared with the SMT degradation in H_2O, the degradation rate of SMT was faster in D_2O (Fig. 5d), indicating that $^1O_2$ was generated in the Fe-PAC-2/PMS system. On the other hand, as a typical quenching agent of $O_2^{\bullet-}$, CF could hardly inhibit the SMT degradation efficiency (Fig. 5a), which could be speculated that $^1O_2$ was not generated from $O_2^{\bullet-}$ in Fe-PAC-2/PMS system [14]. Moreover, only 5 % of the SMT was removed by the individual PMS system (Fig. 3a), which indicated that PMS self-decomposition was a negligible source of $^1O_2$. The foregoing results indicated that the $^1O_2$ in the Fe-PAC-2/PMS system was mainly derived from PMS activation by Fe-PAC-2 [52].

To identify the active sites on Fe-PAC-2, both fresh and used Fe-PAC-2 were analyzed by XPS spectra. As shown in Fig. S11 and Table S9, the contents of Fe^{2+} and C-N/C-O bond decreased from 46.03 % and 30.21–35.51 % and 11.01 %, respectively, while the contents of Fe^{3+} and C=O bond increased, which implied that the Fe-PAC-2 catalyst was oxidized during activation process. The single metal atom was reported to work as electron donor to the PMS molecular to cleave the O-O bond, producing OH* and SO_4^*, and the metal was oxidized [24]. Hence, Fe^{2+} was oxidized to Fe^{3+} after electron transfer to PMS during the activation of PMS. On the other hand, N atoms with a higher electronegativity endowed the adjacent C atoms with a positive charge, which could serve as a potential adsorption site for the intermediate OH* and subsequently activated to generate $^1O_2$. Moreover, due to the strong electron-donating ability of N atoms in the pyrimidine ring of SMT, the electron-deficient C atoms in the C-N configuration (adjacent C atoms of pyrrolic N and pyridinic N) of Fe-PAC could be certainly also served as adsorption site to bind SMT [60]. The red-shift of C-N bond from the C 1 s XPS spectra of the used Fe-PAC-2 (Fig. S11a) further confirmed the adsorption of SMT on Fe-PAC-2. The adsorption mechanism of SMT also covers the pore-filling, which could be verified by the adsorption performance of Fe-PPC and Fe-PAC-2 in Fig. 3a. Therefore, the generated $^1O_2$ could rapidly oxidize the adsorbed SMT within a short diffusion distance, then promoting the removal efficiency of pollutant [61]. Finally, it is reasonable to speculated that Fe^{2+} and C-N were the main active sites for PMS activation, $^1O_2$ production and SMT degradation.

3.5.2. DFT calculation

The possible active sites and pathway towards selective $^1O_2$

generation mechanism was further evaluated by DFT calculations. The optimized structures of PAC and Fe-PAC-2 (Fig. S12) were theoretically modeled based on the materials characterization section. The adsorption and decomposition of PMS on the PAC and Fe-PAC-2 were computational studied. Based on the new insights into the activation of PMS towards $^1O_2$ production, two different reaction pathways were analyzed [37]: 1) the terminal O (O1, Fig. 6a) of PMS was adsorbed on the active sites, which could facilitate the oxidization of PMS to form SO_5^* and then rapidly activated to produce $^1O_2$, SO_4^{2-} and $S_2O_8^{2-}$ (Fig. S13a, Text S6) [14]. 2) The single O atoms (O2, Fig. 6a) of the SO_4 side of PMS was adsorbed on active sites, which was more conducive to the decomposition of PMS into SO_4^* and OH* moieties (Fig. 6c), the OH* was then transformed to produce $^1O_2$ (Text S6) [37]. As shown in Fig. 6a, c and S13b, the Fe sites of Fe-PAC-2 preferentially adsorbed the O2 site of PMS due to the more negative adsorption ($\Delta E_{ads} = -2.37$ eV) and activation energies ($\Delta E_{act} = 1.77$ eV). And thus promoted the decomposition of PMS into SO_4^* and OH* via a completely spontaneous process. Moreover, Bader charge change of cleavage into SO_5^* and H* (0.24 eV) was much lower than that of divided SO_4^* and OH* (0.26 eV), demonstrating that more electron transfer happened between Fe sites and PMS in the second pathway (Fig. S14, Table S12) [24,62]. Fig. 6d witnessed the differential charge density of PMS adsorption on PAC and Fe-PAC-2, where the electrons transferred from PMS to pyrrolic N for PAC and from Fe atom to PMS, respectively. These results indicated that the Fe-PAC-2 act as an electron donor to reduce PMS in the course of PMS activation, while PMS preferred to deliver electrons to PAC. With respect to the intrinsic catalyst properties, Fe-PAC-2 has a substantially smaller electrochemical impedance spectroscopy Nyquist arc diameter than that of PAC (Fig. 5e). This observation verified that the electron migration kinetics and yield were enhanced upon introducing Fe sites into the PAC framework, boosting the formation of reactive species [63]. A noticeable decrease in current for Fe-PAC-2 electrode after the addition of PMS in LSV analysis (Fig. 5f) further evidenced the internal electron migration in the presence of Fe sites [64,65].

To distinguish the different selectivity towards ROSs formation between pyrrolic N sites and single Fe sites, optimized proposed pathway for the $^1O_2$ production were then displayed in Fig. 6c and S13b. Fe-PAC-2 presented adsorption energy of -3.70 eV compared to that for PAC of -2.37 eV (Fig. 6a), demonstrating that the incorporation of single-atom Fe facilitated the adsorption of PMS, and subsequently promoted the activation of PMS due to the negative reaction energy ($\Delta E = -1.35$ eV) than PAC ($\Delta E = 1.77$ eV). After PMS was decomposed into OH* and SO_4^* moieties (Fig. 6c), the dissociative OH* adsorbed onto active sites of catalyst, after the release of H, two possible pathways could happen: pathway 1 was the direct desorption of O* to produce $^1O_2$ (OH*→O*→2 O*→$^1O_2$, Fig. S15a, c). And pathway 2 was the formation of OOH* first, and then removed H to generate $^1O_2$ (OH*→O*→OOH*→$^1O_2$, Fig. 6e and S15b).

The catalytic properties of catalysts were reported synergistically determined by metal-ligand clusters in the first coordination sphere (first-CS) and the binding pocket in the second coordination sphere (second-CS) [66]. The adjacent carbon sites of pyrrolic-N, as the second-CS, were reported to be more susceptible to adsorb intermediates (such as OOH* and OH*) than pyridinic-N and graphitic-N sites [67,68]. Therefore, the adsorbed energy of OH* intermediates on both Fe sites and adjacent C of pyrrolic-N sites and subsequent reactions energy to produce $^1O_2$ were further calculated. As shown in Fig. 6b, e and S15, the overall process from OH* to $^1O_2$ at both active sites required additional energy, whereas when it occurred at the Fe site, the energy barrier to be overcome was lower than C sites, therefore OH* seemed to be more likely to be adsorbed on the Fe sites for subsequent reactions. On the other hand, the pathway of OH* →$^1O_2$ on Fe sites was also calculated (Fig. 6b). It could be concluded that the pathway 2 was thermodynamically inclined to happen for the low energy barrier ($\Delta E = 2.20$ eV), namely, the OH*→O*→OOH*→$^1O_2$ (Fig. 6e) was the reaction pathway for producing $^1O_2$.
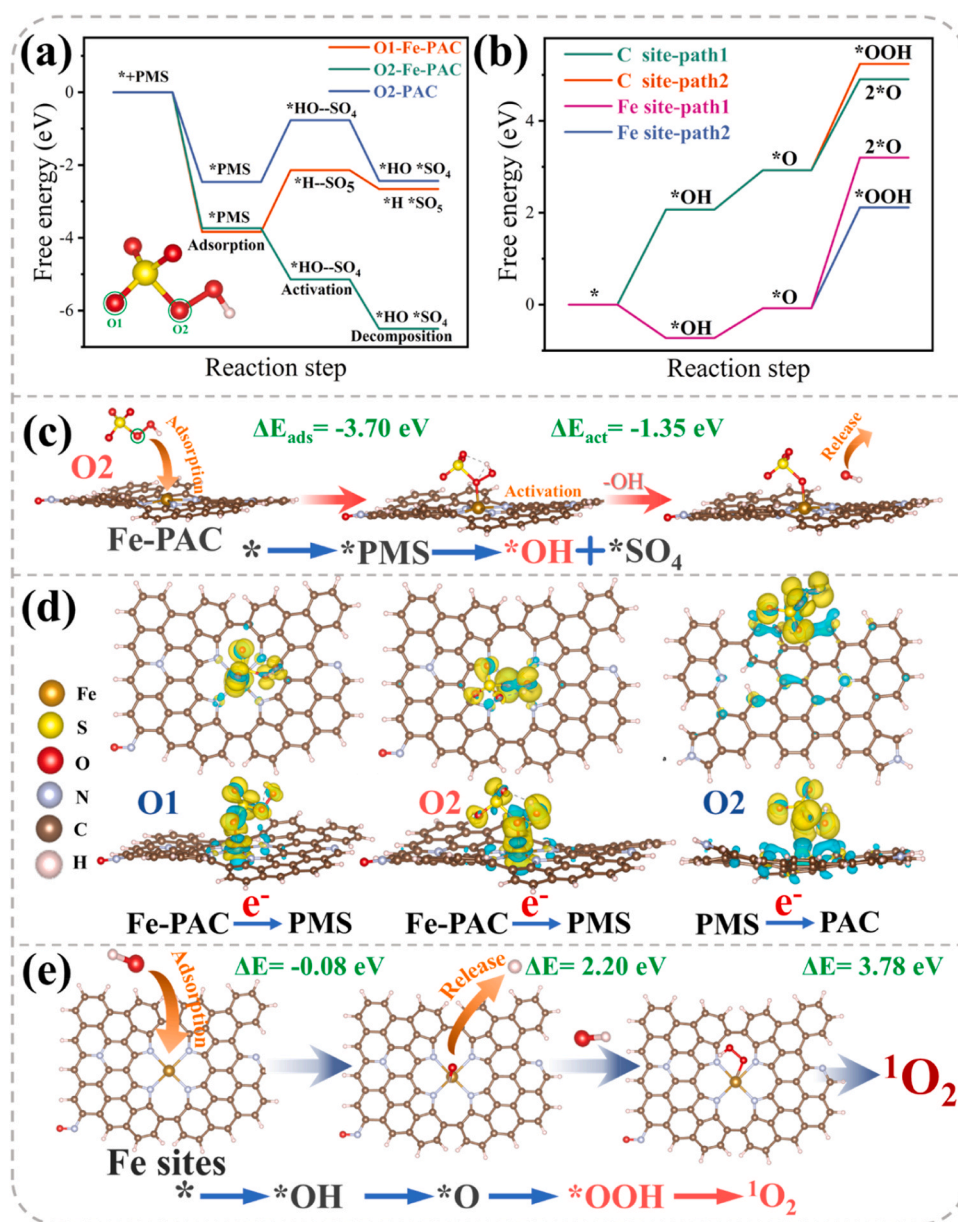
Fig. 6. Proposed mechanism of $^1O_2$ generation for activation PMS on Fe-PAC by DFT methods. (a) free energies comparison of different O site on the Fe-PAC and PAC (inset: molecular model of PMS). (b) free energies of OH* intermediate adsorption and decomposition to $^1O_2$ on different active sites. And schematic diagram of (c) O2 site of the PMS adsorbed on Fe-PAC. (d) differential charge density of PMS adsorption model on different catalysts sites (the yellow and blue isosurfaces represent charge accumulation and depletion respectively). (e)the pathway from *OH to $^1O_2$ on Fe sites in Fe-PAC.

3.6. SMT degradation pathway and toxicity assessment

The intermediate products during the degradation process were determined via UPLC-TOF-MS. Based on the structures and types of the obtained intermediate products (Fig. S16 and S17), a possible degradation pathway of SMT was proposed in Fig. 7a [69]. i) The nitrosation/nitrification of SMT, forming P1 and P4 (SMT→P1→P4). Then P4 underwent the hydroxylation reaction (P4→P9), heterocyclic ring-opening reaction (P4→P8) and a series of similes-type rearrangement reaction followed by SO_2 extrution (P4→P10). Subsequently, these intermediate products (P9, P10) underwent a series of oxidation/deamination/rearrangement reaction followed by SO_2 extrution to generate corresponding P5, P7, P11 and P12. ii) The breakage of N-S bond of SMT led to the formation of P2 and P5, and the products were further deamination/oxidation to generated P6 and P7. iii) SMT experienced strong oxidation at N-S bond as well as desulfonation, deamination, hydroxylation and Smiles rearrangement reactions to produce P13. At last, P3 were accumulated in accordance to the quick oxidation of SMT at the susceptible site. Moreover, the six-heterocyclic ring in SMT products was difficult to be removed during the AOPs process, which could explain the decrease in adsorption performance of the used Fe-PAC-2 [70].

To evaluate the environmental impact of SMT and its degradation products, the ecotoxicity of reaction intermediates generated from Fe-PAC-2/PMS system were estimated via toxicity estimation software tool (T.E.S.T.) on the basis of quantitative structure-activity relationship (QSAR). The LC50 (96 h) of fathead minnow (Fig. 7b) was 56.13 mg L^{-1} for SMT, which categorized as "harmful". And the LC50 (96 h) values of the most intermediates were significantly lower, indicating the acute toxicity of SMT was reduced after degradation. Besides, as shown in Fig. 7c, SMT was classified as the "developmental toxicants" for the developmental toxicity values ≥ 0.5, and the other intermediates exhibited lower developmental toxicity values compared with SMT, suggesting that the degradation intermediates of SMT were less developmentally toxic. In conclusion, the catalytic degradation of SMT by Fe-PAC-2/PMS system seemed to be a more green and low toxic process.

4. Conclusions

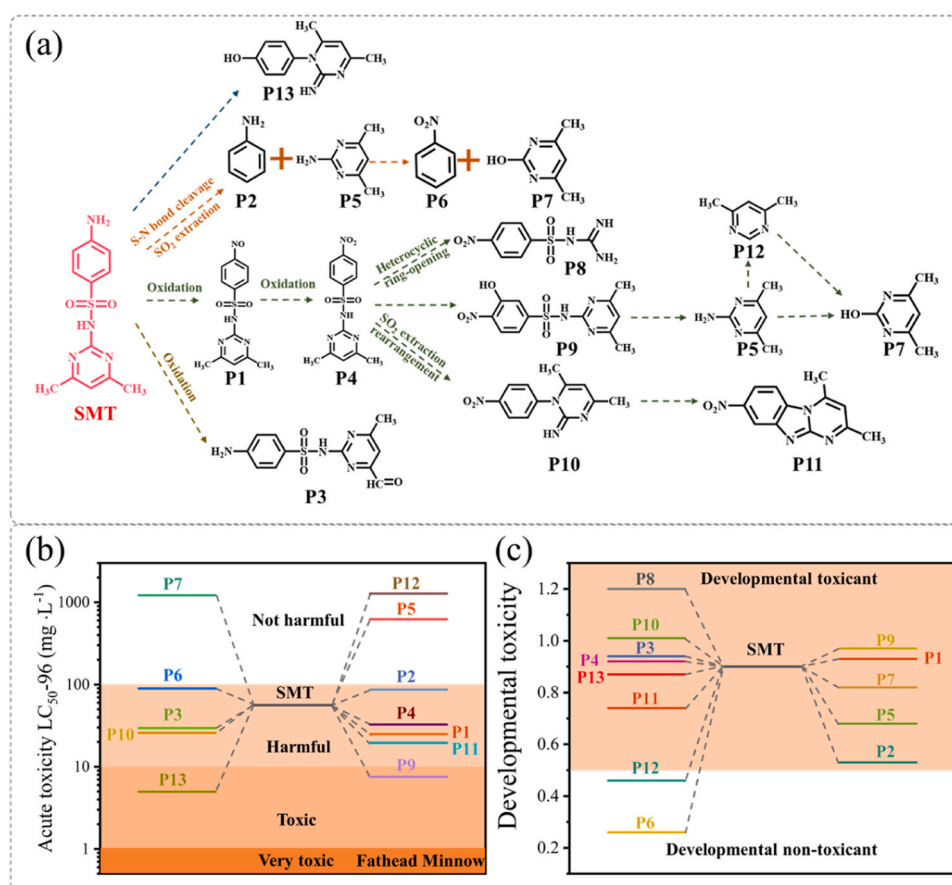In summary, a novel single-atom Fe supported on pyrrolic N-rich

Fig. 7. (a) The proposed degradation pathways of SMZ in the Fe-PAC-2/PMS system. (b) The acute toxicity LC_{50}-96, (c) developmental toxicity of SMT and its possible degradation intermediate products.

catalyst (Fe-PAC) was prepared by using biobased vanillin as building blocks. Fe-PAC-2 exhibited bifunctional performance for high concentration SMT remove via synergistic adsorption and degradation. The ultra-high specific surface area, pyrrolic N-richness and single Fe atoms endowed the Fe-PAC-2/PMS system with high removal capacity (1767.2 mg g^{-1}), as well as wide pH tolerance (3–11), strong resistance to environmental and high selectivity. The ROSs quenching results and EPR signals unveiled that the oxidation capacity of Fe-PAC-2/PMS system mainly relied on $^1O_2$. Theoretical calculations and active site analysis revealed that the Fe and N sites (second-CS) performed different roles: 1) The single Fe atoms acted as main active site for the adsorption and activation of PMS to generate SO$_4$* and OH*. Then the Fe sites adsorbed OH* intermediates and functioned as the active sites for high selectivity $^1O_2$ production. Thus, the reasonable reaction pathway for $^1O_2$ production was PMS → OH* + SO$_4$* → O* → OOH* → $^1O_2$. 2) The adjacent C atoms of pyrrolic N (second-CS) acted as an adsorption site to bind SMT in the vicinity of Fe site, allowing for rapid removal of contaminants. Overall, this work opens up a new perspective for the preparation of single-atom metal catalysts using cost-effective biomass resources and broadens out the avenue for PMS-based AOPs in the treatment of ROPs.

CRediT authorship contribution statement

Yunlong Liu: Methodology, Investigation, Validation, Writing – original draft. **HongYan Zhou:** Visualization, Investigation. **Can Jin:** Conceptualization, Writing – review & editing, Supervision. **Chunmei Tang:** Software. **Wei Zhang:** Data curation, Formal analysis. **Guifeng Liu:** Data curation. **Liang Zhu:** Software. **Fuxiang Chu:** Writing – review & editing, Funding acquisition, Supervision. **Zhenwu Kong:** Writing – review & editing, Funding acquisition, Supervision.

Declaration of Competing Interest

The authors declare that they have no known competing financial interests or personal relationships that could have appeared to influence the work reported in this paper.

Data Availability

Data will be made available on request.

Appendix A. Supporting information

Supplementary data associated with this article can be found in the online version at doi:10.1016/j.apcatb.2023.123061.

References

[1] J. Liang, L. Fu, K. Gao, X. Duan, Accelerating radical generation from peroxymonosulfate by confined variable Co species toward ciprofloxacin mineralization: ROS quantification and mechanisms elucidation, Appl. Catal. B 315 (2022), 121542.

[2] C. di Luca, N. Inchaurrondo, M. Marcé, R. Parra, S. Esplugas, P. Haure, On disclosing the role of mesoporous alumina in the ozonation of sulfamethoxazole: adsorption vs. catalysis, Chem. Eng. J. 412 (2021), 128579.

[3] Y. Chen, X. Bai, Y. Ji, T. Shen, Reduced graphene oxide-supported hollow $Co_3O_4@$ N-doped porous carbon as peroxymonosulfate activator for sulfamethoxazole degradation, Chem. Eng. J. 430 (2022), 132951.

[4] Y. Li, H. Dong, L. Li, J. Xiao, S. Xiao, Z. Jin, Efficient degradation of sulfamethazine via activation of percarbonate by chalcopyrite, Water Res. 202 (2021), 117451.

[5] M. Conde-Cid, R. Cela-Dablanca, G. Ferreira-Coelho, D. Fernandez-Calvino, A. Nunez-Delgado, M.J. Fernandez-Sanjurjo, M. Arias-Estevez, E. Alvarez-Rodriguez, Sulfadiazine, sulfamethazine and sulfachloropyridazine removal using three different porous materials: Pine bark, "oak ash" and mussel shell, Environ. Res. 195 (2021), 110814.

[6] B.J. Shi, Y. Wang, Y.K. Geng, R.D. Liu, X.R. Pan, W.W. Li, G.P. Sheng, Application of membrane bioreactor for sulfamethazine-contained wastewater treatment, Chemosphere 193 (2018) 840–846.

[7] M.K. Panjwani, Q. Wang, Y. Ma, Y. Lin, F. Xiao, S. Yang, High degradation efficiency of sulfamethazine with the dual-reaction-center $Fe-Mn-SiO_2$ Fenton-like nanocatalyst in a wide pH range, Environ. Sci.: Nano 8 (2021) 2204–2213.

[8] D.T. Oyekunle, E.A. Gendy, J. Ifthikar, Z. Chen, Heterogeneous activation of persulfate by metal and non-metal catalyst for the degradation of sulfamethazole: a review, Chem. Eng. J. 437 (2022), 135277.

[9] L. Wu, T. Wu, Z. Liu, W. Tang, S. Xiao, B. Shao, Q. Liang, Q. He, Y. Pan, C. Zhao, Y. Liu, S. Tong, Carbon nanotube-based materials for persulfate activation to degrade organic contaminants: properties, mechanisms and modification insights, J. Hazard. Mater. 431 (2022), 128536.

[10] Y. Xiong, H. Li, C. Liu, L. Zheng, C. Liu, J.O. Wang, S. Liu, Y. Han, L. Gu, J. Qian, D. Wang, Single-atom Fe catalysts for Fenton-like reactions: roles of different N species, Adv. Mater. 34 (2022), e2110653.

[11] J. Wang, B. Li, Y. Li, X. Fan, F. Zhang, G. Zhang, W. Peng, Facile synthesis of atomic Fe-N-C materials and dual roles investigation of $Fe-N_4$ sites in Fenton-like reactions, Adv. Sci. (2021), e2101824.

[12] J. Lee, U. von Gunten, J.H. Kim, Persulfate-based advanced oxidation: critical assessment of opportunities and roadblocks, Environ. Sci. Technol. 54 (2020) 3064–3081.

[13] L. Tian, P. Chen, X.H. Jiang, L.S. Chen, L.L. Tong, H.Y. Yang, J.P. Fan, D.S. Wu, J. P. Zou, S.L. Luo, Mineralization of cyanides via a novel Electro-Fenton system generating •OH and •O_2^{2-}, Water Res. 209 (2021), 117890.

[14] L.S. Zhang, X.H. Jiang, Z.A. Zhong, L. Tian, Q. Sun, Y.T. Cui, X. Lu, J.P. Zou, S. L. Luo, Carbon nitride supported high-loading Fe single-atom catalyst for activation of peroxymonosulfate to generate $^1O_2$ with 100 % selectivity, Angew. Chem. Int. Ed. Engl. 60 (2021) 21751–21755.

[15] X. Mi, P. Wang, S. Xu, L. Su, H. Zhong, H. Wang, Y. Li, S. Zhan, Almost 100 % peroxymonosulfate conversion to singlet oxygen on single-atom CoN_{2+2} sites, Angew. Chem. Int. Ed. Engl. 133 (2021) 4638–4643.

[16] Y. Bu, H. Li, W. Yu, Y. Pan, L. Li, Y. Wang, L. Pu, J. Ding, G. Gao, B. Pan, Peroxydisulfate activation and singlet oxygen generation by oxygen vacancy for degradation of contaminants, Environ. Sci. Technol. 55 (2021) 2110–2120.

[17] D. Wang, M. Suo, S. Lai, L. Deng, J. Liu, J. Yang, S. Chen, M.F. Wu, J.P. Zou, Photoinduced acceleration of Fe^{3+}/Fe^{2+} cycle in heterogeneous FeNi-MOFs to boost peroxodisulfate activation for organic pollutant degradation, Appl. Catal. B 321 (2023), 122054.

[18] Y. Qi, J. Li, Y. Zhang, Q. Cao, Y. Si, Z. Wu, M. Akram, X. Xu, Novel lignin-based single atom catalysts as peroxymonosulfate activator for pollutants degradation: Role of single cobalt and electron transfer pathway, Appl. Catal. B 286 (2021), 119910.

[19] Q.Z. Shu Cai, Ziqian Wang, Sheng Hua, Dahu Ding, Tianming Cai, Ruihong Zhang, Pyrrolic N-rich, biochar without exogenous nitrogen doping as a functional material for bisphenol A removal: performance and mechanism, Appl. Catal. B 291 (2022), 120093.

[20] Z. Pi, K. Hou, F. Yao, L. He, S. Chen, Z. Tao, P. Zhou, D. Wang, X. Li, Q. Yang, In-situ regeneration of tetracycline-saturated hierarchical porous carbon by peroxydisulfate oxidation process: performance, mechanism and application, Chem. Eng. J. 427 (2022), 131749.

[21] B. Huang, Z. Wu, H. Zhou, J. Li, C. Zhou, Z. Xiong, Z. Pan, G. Yao, B. Lai, Recent advances in single-atom catalysts for advanced oxidation processes in water purification, J. Hazard. Mater. 412 (2021), 125253.

[22] X.H. Jiang, L.S. Zhang, H.Y. Liu, D.S. Wu, F.Y. Wu, L. Tian, L.L. Liu, J.P. Zou, S. L. Luo, B.B. Chen, Silver single atom in carbon nitride catalyst for highly efficient photocatalytic hydrogen evolution, Angew. Chem. Int. Ed. Engl. 59 (2020) 23112–23116.

[23] X. Wu, H. Zhang, S. Zuo, J. Dong, Y. Li, J. Zhang, Y. Han, Engineering the coordination sphere of isolated active sites to explore the intrinsic activity in single-atom catalysts, Nano-Micro Lett. 13 (2021) 136.

[24] Z. Wang, E. Almatrafi, H. Wang, H. Qin, W. Wang, L. Du, S. Chen, G. Zeng, P. Xu, Cobalt single atoms anchored on oxygen-doped tubular carbon nitride for efficient peroxymonosulfate activation: simultaneous coordination structure and morphology modulation, Angew. Chem. Int. Ed. Engl. (2022), e202202338.

[25] X. Li, X. Huang, S. Xi, S. Miao, J. Ding, W. Cai, S. Liu, X. Yang, H. Yang, J. Gao, J. Wang, Y. Huang, T. Zhang, B. Liu, Single cobalt atoms anchored on porous N-doped graphene with dual reaction sites for efficient fenton-like catalysis, J. Am. Chem. Soc. 140 (2018) 12469–12475.

[26] X. Zhao, X. Jia, H. Li, H. Zhang, X. Zhou, Y. Zhou, H. Wang, L. Yin, T. Wågberg, G. Hu, Efficient degradation of Health-threatening organic pollutants in water by atomically dispersed Cobalt-Activated peroxymonosulfate, Chem. Eng. J. 450 (2022), 138098.

[27] H. Zhang, J. Deng, Y. Wu, Biobased magnetic microspheres containing aldehyde groups: constructed by vanillin-derived polymethacrylate/Fe_3O_4 and recycled in adsorbing amine, ACS Sustain. Chem. Eng. 5 (2016) 658–666.

[28] Z. Wang, P. Gnanasekar, S. Sudhakaran Nair, R. Farnood, S. Yi, N. Yan, Biobased epoxy synthesized from a Vanillin derivative and its reinforcement using lignin-containing cellulose nanofibrils, ACS Sustain. Chem. Eng. 8 (2020) 11215–11223.

[29] Y. Liu, C. Jin, Z. Yang, G. Wu, G. Liu, Z. Kong, Recent advances in lignin-based porous materials for pollutants removal from wastewater, Int. J. Biol. Macromol. 187 (2021) 880–891.

[30] Y. Liu, X. Zhou, C. Jin, G. Liu, Z. Liu, Z. Kong, Efficient and rapid removal of typical phenolic compounds from water with biobased porous organic polymers, Ind. Crops Prod. 184 (2022), 114971.

[31] A. Modak, M. Pramanik, S. Inagaki, A. Bhaumik, A triazine functionalized porous organic polymer: excellent CO_2 storage material and support for designing Pd nanocatalyst for C–C cross-coupling reactions, J. Mater. Chem. A 2 (2014) 11642.

[32] D. Li, Y. Fang, X. Zhang, Bacterial detection and elimination using a dual-functional porphyrin-based porous organic polymer with peroxidase-like and high near-infrared-light-enhanced antibacterial activity, ACS Appl. Mater. Interfaces 12 (2020) 8989–8999.

[33] Y. Zou, J. Hu, B. Li, L. Lin, Y. Li, F. Liu, Xy Li, Tailoring the coordination environment of cobalt in a single-atom catalyst through phosphorus doping for enhanced activation of peroxymonosulfate and thus efficient degradation of sulfadiazine, Appl. Catal. B 312 (2022), 121408.

[34] L. Xie, Z. Zheng, Q. Lin, H. Zhou, X. Ji, J.L. Sessler, H. Wang, Calix[4]pyrrole-based crosslinked polymer networks for highly effective iodine adsorption from water, Angew. Chem. Int. Ed. 61 (2022), e202113724.

[35] L. Liu, S. Jayakumar, J. Chen, L. Tao, H. Li, Q. Yang, C. Li, Synthesis of bifunctional porphyrin polymers for catalytic conversion of dilute CO_2 to cyclic carbonates, ACS Appl. Mater. Interfaces (2021) 29522–29531.

[36] C. Cheng, S. Li, Y. Xia, L. Ma, C. Nie, C. Roth, A. Thomas, R. Haag, Atomic Fe-Nx coupled open-mesoporous carbon nanofibers for efficient and bioadaptable oxygen electrode in Mg-Air batteries, Adv. Mater. (2018), e1802669.

[37] Y. Gao, T. Wu, C. Yang, C. Ma, Z. Zhao, Z. Wu, S. Cao, W. Geng, Y. Wang, Y. Yao, Y. Zhang, C. Cheng, Activity trends and mechanisms in peroxymonosulfate-assisted catalytic production of singlet oxygen over atomic metal-N-C catalysts, Angew. Chem. Int. Ed. Engl. 60 (2021) 22513–22521.

[38] C. Ding, Z. Liu, S. Pan, C. Zhao, Z. Wang, B. Gao, Q. Li, Activation of peroxydisulfate via Fe@sulfur-doped carbon-supported nanocomposite for degradation of norfloxacin: efficiency and mechanism, Chem. Eng. J. 460 (2023), 141729.

[39] L. Yang, H. Yang, S. Yin, X. Wang, M. Xu, G. Lu, Z. Liu, H. Sun, Fe single-atom catalyst for efficient and rapid fenton-like degradation of organics and disinfection against bacteria, Small 18 (2022), e2104941.

[40] X. Peng, J. Wu, Z. Zhao, X. Wang, H. Dai, L. Xu, G. Xu, Y. Jian, F. Hu, Activation of peroxymonosulfate by single-atom $Fe-g-C_3N_4$ catalysts for high efficiency degradation of tetracycline via nonradical pathways: Role of high-valent iron-oxo species and Fe-Nx sites, Chem. Eng. J. 427 (2022), 130803.

[41] Y.C. Lee, Y.F. Li, S.L. Lo, J. Kuo, W. Sun, C.Y. Hu, Decomposition of perfluorooctanic acid by carbon aerogel with persulfate, Chem. Eng. J. 430 (2022), 132900.

[42] R. Deng, H. Luo, D. Huang, C. Zhang, Biochar-mediated Fenton-like reaction for the degradation of sulfamethazine: role of environmentally persistent free radicals, Chemosphere 255 (2020), 126975.

[43] S. Xiang, H. Dong, Y. Li, J. Xiao, Q. Dong, X. Hou, D. Chu, A comparative study of activation of peroxymonosulfate and peroxydisulfate by greigite (Fe_3S_4) for the degradation of sulfamethazine in water, Sep. Purif. Technol. 290 (2022), 120873.

[44] C. Chen, L. Liu, Y. Li, W. Li, L. Zhou, Y. Lan, Y. Li, Insight into heterogeneous catalytic degradation of sulfamethazine by peroxymonosulfate activated with $CuCo_2O_4$ derived from bimetallic oxalate, Chem. Eng. J. 384 (2020), 123257.

[45] Q. Sun, X. Wang, Y. Liu, S. Xia, J. Zhao, Activation of peroxymonosulfate by a floating oxygen vacancies - $CuFe_2O_4$ photocatalyst under visible light for efficient degradation of sulfamethazine, Sci. Total Environ. 824 (2022), 153630.

[46] H. Jiang, C. Zhu, Y. Yuan, C. Yue, C. Ling, F. Liu, A. Li, Enhanced activation of peroxymonosulfate with metal-substituted hollow $MxCo_3-xS_4$ polyhedrons for superfast degradation of sulfamethazine, Chem. Eng. J. 384 (2020), 123302.

[47] M. Yu, X. Mao, X. He, M. Zheng, X. Zhang, J. Su, B. Xi, Efficient degradation of sulfamethazine in a silicified microscale zero-valent iron activated persulfate process, Appl. Catal. B 312 (2022), 121418.

[48] Y. Pan, Z. Bu, J. Li, W. Wang, G. Wu, Y. Zhang, Sulfamethazine removal by peracetic acid activation with sulfide-modified zero-valent iron: efficiency, the role of sulfur species, and mechanisms, Sep. Purif. Technol. 277 (2021), 119402.

[49] D. Chu, H. Dong, Y. Li, Z. Jin, J. Xiao, S. Xiang, Q. Dong, X. Hou, Enhanced activation of sulfite by a mixture of zero-valent Fe-Mn bimetallic nanoparticles and biochar for degradation of sulfamethazine in water, Sep. Purif. Technol. 285 (2022), 120315.

[50] Z. Bai, Q. Yang, J. Wang, Catalytic ozonation of sulfamethazine using $Ce0.1Fe0.9OOH$ as catalyst: mineralization and catalytic mechanisms, Chem. Eng. J. 300 (2016) 169–176.

[51] C. Fu, X. Yi, Y. Liu, H. Zhou, Cu^{2+} activated persulfate for sulfamethazine degradation, Chemosphere 257 (2020), 127294.

[52] H. Fu, H. Luo, Q. Lin, Q. Zhong, Z. Huang, Y. Wang, L. Wu, Transformation to nonradical pathway for the activation of peroxydisulfate after doping S into Fe_3C-encapsulated N/S-codoped carbon nanotubes, Chem. Eng. J. 409 (2021), 128201.

[53] Y. Bao, C. Lian, K. Huang, H. Yu, W. Liu, J. Zhang, M. Xing, Generating high-valent iron-oxo identical with Fe(IV)=O complexes in neutral microenvironments through peroxymonosulfate activation by Zn-Fe layered double hydroxides, Angew. Chem. Int. Ed. Engl. 61 (2022), e202209542.

[54] X. Liu, X. Yan, W. Liu, Q. Yan, M. Xing, Switching of radical and nonradical pathways through the surface defects of Fe_3O_4/MoO_xS_y in a Fenton-like reaction, Sci. Bull. 68 (2023) 603–612.

[55] N. Li, R. Li, X. Duan, B. Yan, W. Liu, Z. Cheng, G. Chen, L. Hou, S. Wang, Correlation of active sites to generated reactive species and degradation routes of organics in peroxymonosulfate activation by Co-loaded carbon, Environ. Sci. Technol. (2021) 16163–16174.

[56] N. Du, Y. Liu, Q. Li, W. Miao, D. Wang, S. Mao, Peroxydisulfate activation by atomically-dispersed Fe-Nx on N-doped carbon: mechanism of singlet oxygen evolution for nonradical degradation of aqueous contaminants, Chem. Eng. J. 413 (2021), 127545.

[57] E.-T. Yun, S.-W. Park, H.J. Shin, H. Lee, D.-W. Kim, J. Lee, Peroxymonosulfate activation by carbon-encapsulated metal nanoparticles: switching the primary reaction route and increasing chemical stability, Appl. Catal. B 279 (2020), 119360.

[58] Z.Y. Choong, M.F. Gasim, K.-Y.A. Lin, T.S. Hamidon, H. Hussin, W.D. Oh, Unravelling the formation mechanism and performance of nitrogen, sulfur codoped biochar as peroxymonosulfate activator for gatifloxacin removal, Chem. Eng. J. 451 (2023), 138958.

[59] Y. Yang, P. Zhang, K. Hu, X. Duan, Y. Ren, H. Sun, S. Wang, Sustainable redox processes induced by peroxymonosulfate and metal doping on amorphous manganese dioxide for nonradical degradation of water contaminants, Appl. Catal. B 286 (2021) 11930.

[60] Y. Wang, Z. Zhang, Z. Yin, Z. Liu, Y. Liu, Z. Yang, W. Yang, Adsorption and catalysis of peroxymonosulfate on carbocatalysts for phenol degradation: the role of pyrrolic-nitrogen, Appl. Catal. B 319 (2022), 121891.

[61] S.K. Singh, K. Takeyasu, J. Nakamura, Active sites and mechanism of oxygen reduction reaction electrocatalysis on nitrogen-doped carbon materials, Adv. Mater. 31 (2019), e1804297.

[62] H. Jin, P. Li, P. Cui, J. Shi, W. Zhou, X. Yu, W. Song, C. Cao, Unprecedentedly high activity and selectivity for hydrogenation of nitroarenes with single atomic Co_1-N_3P_1 sites, Nat. Commun. 13 (2022) 723.

[63] X. Liang, D. Wang, Z. Zhao, T. Li, Z. Chen, Y. Gao, C. Hu, Engineering the low-coordinated single cobalt atom to boost persulfate activation for enhanced organic pollutant oxidation, Appl. Catal. B 303 (2022), 120877.

[64] Q. Zhong, C. Xu, Y. Liu, Q. Ji, Z. Xu, D. Sun, S. Zhou, B. Yang, Y. Dai, C. Qi, S. Yang, H. He, S. Li, C. Sun, Defect-engineered $FeSe_2$-x@C with porous architecture for enhanced peroxymonosulfate-based advanced oxidation processes, Appl. Catal. B 309 (2022), 121259.

[65] F. Chen, L.L. Liu, J.H. Wu, X.H. Rui, J.J. Chen, Y. Yu, Single-atom iron anchored tubular g-C_3N_4 catalysts for ultrafast Fenton-like reaction: roles of high-valency iron-oxo species and organic radicals, Adv. Mater. 34 (2022), e2202891.

[66] C. Tang, L. Chen, H. Li, L. Li, Y. Jiao, Y. Zheng, H. Xu, K. Davey, S.Z. Qiao, Tailoring acidic oxygen reduction selectivity on single-atom catalysts via modification of first and second coordination spheres, J. Am. Chem. Soc. 143 (2021) 7819–7827.

[67] D. Guo, R. Shibuya, C. Akiba, S. Saji, T. Kondo, J. Nakamura, Active sites of nitrogen-doped carbon materials for oxygen reduction reaction clarified using model catalysts, Science 351 (2016) 361–365.

[68] D. Iglesias, A. Giuliani, M. Melchionna, S. Marchesan, A. Criado, L. Nasi, M. Bevilacqua, C. Tavagnacco, F. Vizza, M. Prato, P. Fornasiero, N-doped graphitized carbon nanohorns as a forefront electrocatalyst in highly selective O_2 reduction to H_2O_2, Chem 4 (2018) 106–123.

[69] E.L. Schymanski, J. Jeon, R. Gulde, K. Fenner, M. Ruff, H.P. Singer, J. Hollender, Identifying small molecules via high resolution mass spectrometry: communicating confidence, Environ. Sci. Technol. 48 (2014) 2097–2098.

[70] R. Yin, W. Guo, H. Wang, J. Du, X. Zhou, Q. Wu, H. Zheng, J. Chang, N. Ren, Enhanced peroxymonosulfate activation for sulfamethazine degradation by ultrasound irradiation: Performances and mechanisms, Chem. Eng. J. 335 (2018) 145–153.